aerospace

MDPI

Article

The Electrostatic Induction Characteristics of SiC/SiC Particles in Aero-Engine Exhaust Gases: A Simulated Experiment and Analysis

Yan Liu [1,2], Zhenzhen Liu [1,2,*], Fang Bai [3], Hongfu Zuo [1], Zezhong Guo [1] and Xin Li [4]

[1] College of Civil Aviation, Nanjing University of Aeronautics and Astronautics, Nanjing 210016, China; jiayinly@nuaa.edu.cn (Y.L.); rms@nuaa.edu.cn (H.Z.); airrrr@nuaa.edu.cn (Z.G.)
[2] Department of Mechanical and Mechatronics Engineering, The University of Auckland, Auckland 1010, New Zealand
[3] Nanjing Research Institute of Electronic Engineering, Nanjing 210023, China; baifang@cetc.com.cn
[4] School of Automotive & Rail Transit, Nanjing Institute of Technology, Nanjing 211167, China; lixin1990@nuaa.edu.cn
* Correspondence: lzz1201@nuaa.edu.cn

Abstract: This study investigates the electrostatic induction characteristics of silicon carbide-fiber-reinforced silicon carbide (SiC/SiC) particles within aero-engine exhaust gases using a dedicated J20 turbojet engine experimental platform. Our comprehensive experiments explored the electrostatic properties of SiC/SiC particles under varying engine operational states—specifically focusing on different thermal conditions, particle mass concentrations, particle sizes, and exhaust gas velocities compared to those of common engine exhaust constituents like carbon (C) and iron (Fe) particles. The results demonstrate that SiC/SiC particles consistently maintain a stable positive charge across varied temperatures, significantly diverging from the behaviors of carbon (C) and iron (Fe) particles. Additionally, our findings reveal that higher mass concentrations of SiC/SiC particles, smaller particle sizes within a certain range, and greater exhaust gas velocities of the aero-engine all lead to increased particle charge and more pronounced electrostatic induction characteristics. This study highlights the potential of electrostatic sensors for the early detection and diagnosis of failures in aero-engines, offering crucial insights into the development of more resilient real-time aero-engine health monitoring systems.

Keywords: electrostatic sensor; ceramic matrix composites (CMCs); aero-engine fault diagnosis; electrostatic characteristics; real-time monitoring

check for updates

Citation: Liu, Y.; Liu, Z.; Bai, F.; Zuo, H.; Guo, Z.; Li, X. The Electrostatic Induction Characteristics of SiC/SiC Particles in Aero-Engine Exhaust Gases: A Simulated Experiment and Analysis. *Aerospace* **2024**, *11*, 481. https://doi.org/10.3390/aerospace11060481

Academic Editor: Konstantinos Tserpes

Received: 26 March 2024
Revised: 24 May 2024
Accepted: 11 June 2024
Published: 17 June 2024

Copyright: © 2024 by the authors. Licensee MDPI, Basel, Switzerland. This article is an open access article distributed under the terms and conditions of the Creative Commons Attribution (CC BY) license (https://creativecommons.org/licenses/by/4.0/).

1. Introduction

Due to its high-temperature capability and excellent wear and corrosion resistance [1], silicon carbide-fiber-reinforced silicon carbide (SiC/SiC), a ceramic matrix composite (CMC) material, is regarded by the National Aeronautics and Space Administration (NASA) as the most promising material for the hot-section components of modern aero-engines [2,3] and has been successfully applied to aero-engine components such as turbofans [4], rotor blades [5], and combustion chambers [6]. These SiC/SiC hot-section components usually operate at elevated temperatures and high pressures and in intense mechanical strain environments, which readily predispose these components to mechanical issues, leading to a subsequent deterioration in performance. Ensuring hot-section components' robust health and optimal functioning is pivotal for flight safety, attracting considerable research into effective condition monitoring methods.

The condition monitoring technologies for these hot-section components include offline and real-time methods. Offline methods predominantly rely on X-ray analysis [7], infrared thermal imaging [7], industrial computed tomography (CT) [7], ultrasonic testing [8], resistance monitoring [9], and acoustic emission detection [10]. However, these

monitoring techniques fail to meet the real-time monitoring demands posed by contemporary engine Prognostics and Health Management (PHM) technology [11]. In contrast, the traditional real-time methods primarily utilize vibration [12] and gas path performance parameters [13]. Nevertheless, conventional real-time monitoring techniques' constrained early warning capability is a notable limitation, as these methods can only identify faults in gas path components after they have already manifested in the signal [14].

To address these drawbacks, researchers have exhibited a heightened interest in electrostatic monitoring technology, a real-time approach with the potential to predict early engine gas path component faults [15]. Compared to indirect monitoring using traditional methods, the electrostatic monitoring technique can directly detect particles released into the exhaust gas due to engine wear, making it more sensitive to early faults [16,17]. Within the investigation of electrostatic monitoring technology, extensive research has been dedicated to various facets, including the mechanism itself [18,19], the application of the electrostatic field model to exhaust particles [20], the development of induction models for sensors [21,22], pertinent measurement techniques [23–25], and electrostatic monitoring experiments [26–30].

When engine components are distressed, such as turbines or combustion, abnormal particles in the engine exhaust gas will appear. The particles generated by these components constitute a critical focus in electrostatic monitoring research because the charged properties of these particles, such as their charged polarity and magnitude of charge, have the potential to reveal faults within engine components. Investigating the electrostatic induction characteristics of particles originating from various materials in the engine gas path enables analysis of the intrinsic connection between the material properties, charging characteristics, and the quantity of electrostatic charge in the engine exhaust. These intrinsic connections offer the possibility for real-time classification of the particles in the exhaust. When abnormalities are detected in real time, the electrostatic induction characteristics of the particles become crucial in determining material wear properties. The combination of time domain parameters, the activity rate level, and other characteristic parameters is beneficial in aiding the early detection of abnormal components in the engine gas path and provides valuable reference information for engine fault diagnosis.

In recent years, researchers have shown an increased interest in detecting particles' electrostatic characteristics for engine health monitoring. Papers [31,32] investigated the electrostatic induction properties of metal particles such as iron (Fe) and aluminum (Al) using electrostatic monitoring techniques in the exhaust gases of rocket motors. The results proved that these experiments were very effective in monitoring combustion instability and detecting metal ions, which provided a foundation for identifying potential precursors to combustion instability and engine failures. Paper [33] investigates the formation mechanism and detection of charged particles in the aero-engine gas path, focusing on the electrostatic induction characteristics of carbon (C) particles. The experimental findings reveal that larger particles induce more significant charge amplitudes, offering robust support for identifying abnormal particle types. Paper [34] focuses on the electrostatic induction characteristics of metal particles, specifically C and Fe, within the aero-engine gas path. By simulating the larger-sized metal particles produced during engine blade rub faults, this study elucidates the contrasting polarity characteristics of metal particles compared to carbon particles through analysis of electrostatic monitoring signals. Moreover, the article validates the influence of the engine operating conditions on charge quantity through engine tests, affirming the practical applicability of electrostatic monitoring technology for real-time tracking of engine condition variations.

However, the research has mainly focused on the electrostatic properties of metallic Fe and non-metallic C particles. Understanding the electrostatic induction characteristics of ceramic matrix composite (CMC) materials such as SiC/SiC particles in engine exhaust is crucial for developing advanced engines using real-time electrostatic monitoring technology. Despite its significance, more research is currently needed in this specific domain. Experimental verification becomes imperative given the intricate nature of particle

charging principles in engine exhaust. Therefore, a comprehensive investigation of the electrostatic characteristics of SiC/SiC particles (composite material) in engine exhaust is required. However, direct electrostatic monitoring experiments on SiC/SiC component failure within an engine are both destructive and costly. Consequently, it is imperative to conduct laboratory-simulated experiments beforehand to delineate the electrostatic induction characteristics of SiC/SiC particles, gather empirical data, and establish a theoretical foundation for subsequent bench experiments and in-flight airborne experiments.

This study systematically explores the electrostatic induction characteristics of SiC/SiC particles and their influencing factors in aero-engine exhaust gases. Initially, a dedicated J20 turbojet engine experimental platform with an electrostatic sensor system was developed to conduct simulated fault diagnoses and monitoring tests for SiC/SiC particles. Subsequently, single-variable comparison experiments were performed, varying the engine exhaust gas temperature, particle concentration, particle size, and exhaust gas velocity. Under the different variable conditions, the electrostatic induction signals generated by SiC/SiC charged particles in the engine exhaust were then collected. Then, a comparative analysis was performed on crucial characteristic parameters, including peak value, RMS value, and positive and negative event rate, for each group of experimental signals. Notably, the findings underscore the varying influences of the three variable conditions on different characteristic parameters of SiC/SiC particles' electrostatic induction signals.

Additionally, the results were compared with those signals obtained from C and Fe particles, which are common in engine exhaust gas. Of particular significance is the discovery that SiC/SiC particles exhibit a stable positive charge following both cold engine operation and combustion conditions, a distinctive feature diverging from the electrostatic properties of C and Fe particles. Consequently, the positive event rate emerges as a promising feature for detecting faults in SiC/SiC components during engine fault monitoring. This study demonstrates the feasibility of identifying abnormal SiC/SiC particles in engine exhaust monitoring and establishes a research foundation for further exploration into the electrostatic identification of particulates in aero-engines.

The remainder of this paper is structured as follows: In Section 2, we introduce the principles of the fundamentals of electrostatic monitoring. Section 3 offers detailed information on the experiments and the data process methodologies utilized in our research. Section 4 contains the experimental results and a comprehensive comparative analysis. Finally, we conclude our paper in Section 5.

2. Fundamentals of Electrostatic Monitoring

2.1. Sources of Aero-Engine Exhaust Charged Particles

The sources of aero-engine exhaust particles are mainly divided into ordinary combustion carbon particles and abnormal particles. In normal combustion, carbon particles arise primarily due to the polymerization of hydrocarbons with ions and nuclei in the flame zone of the combustion chamber to form carbon soot particles [33]. In addition to the abnormal particles produced by failures of the gas path components such as intake tract inhalation of foreign materials, blade ablation, normal combustion, coating flaking, loss of material due to cyclic stresses locally on the blade in a high-temperature environment, and friction between the blade and the housing are possible sources of abnormal particles in the exhaust gas [15,35].

2.2. The Electrostatic Charging Mechanism of Aero-Engine Exhaust Particles

In the aero-engine combustion chamber, due to the fuel combustion generated by the high temperature of the gas molecules undergoing a chemical ionization reaction, the kinetic energy of the gas molecules is proportional to the temperature. When the temperature increases, the average kinetic energy increases, greater than the ionization energy of the gas molecules, which also increases dramatically. When there is a significant increase in the collision between the gas molecules, this can cause the gas molecules to become unstable. When sufficient kinetic energy exists in the electrons, unstable atoms, or

ions, the colliding gas molecules or compounds may be dissociated into dissociated atoms, free atom groups, molecular ions, and dissociated atoms.

When soot particles form in the oil-rich zone and pass through the high-temperature flame zone, chemical ionization of these gases results in numerous charged ions filling the entire gas path. This is caused by the formation of a chemical ionization reaction of free electrons, ions, and particles charged by interaction [20]. Soot particles produced by combustion can acquire an electric charge when they are hit with ions traveling randomly and thermally. The mechanism may be described as follows [33]:

$$q_P = \frac{d_p kT}{2e^2} \ln\left(1 + \frac{d_p c \pi^2 N t}{2kT}\right) \quad (1)$$

where q_p is the charged number of particles (pC), d_p is the diameter of the particles (m), k is Boltzmann's constant (1.38×10^{-23} J/K), T is the temperature (K), e is the charge of the electrons (1.6×10^{-19} C), c is the average velocity of the particles (m/s), N is the concentration of the particles (ions/m^3), and t is the time (s).

Qualitatively, it can be seen from Equation (1) that the electric charge of the particles is mainly related to the particle size and temperature, and the particle concentration and particle velocity also affect the charge of the particles.

Solid particles are also charged by contact charging, separation charging, friction charging, and fracture charging. These electric charging modes are manifested in the operating environment of the aero-engine gas path, such as friction between the blades and housing, particle–wall and particle–particle collisions, and material loss due to erosion.

2.3. Principles of Electrostatic Sensing

Figure 1 depicts the charge detection process in an electrostatic sensor as a moving charge particle traverses the sensor's surface [36]. When the charged particle passes across the surface of the electrostatic sensor, electric (E-) field lines due to the charge (+Q) terminate on the sensor face. The electrons in the sensor redistribute to balance the additional charge in the vicinity of the sensor, inducing opposite charges and resulting in a current flow, which is measured by a conditioner. The signal conditioning transforms the observed charge into a proportionate voltage signal that is collected and analyzed [37].

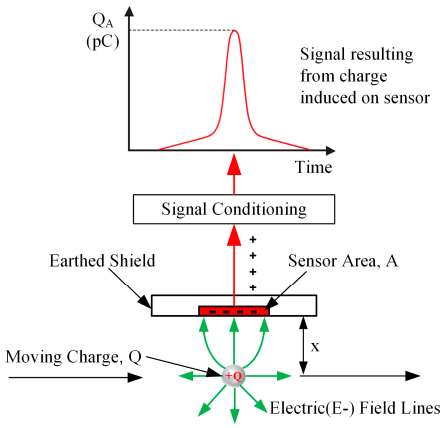


Figure 1. Illustration of the electrostatic sensing mechanism.

As a result of the limited size of the sensor, some of the electric field lines will not end on the sensor surface, and hence, not all of the charge Q will be detected. The relationship between the quantity of charge sensed by the sensor, Q_A, may be estimated as follows:

$$Q_A \sim \frac{QA}{x^2} \quad (2)$$

where A is the sensor area, and x is the distance between the charged particle and the sensor face.

Equation (2) shows that the sensitivity to charge is directly proportional to the magnitude of the charge and the area of the sensor face, while it is inversely proportional to the distance between the charge and the sensor. The insulating properties of the conveying medium will impact the retention of charge on the moving particle. The enhanced conductivity of the medium will amplify the discharge of charge from the particle, thereby diminishing the remaining charge on the particle.

2.4. Electrostatic Sensor

The Key Laboratory of Civil Aviation Aircraft Health Monitoring and Intelligent Maintenance of Nanjing University of Aeronautics and Astronautics developed the electrostatic sensors used in this paper. The sensor is a non-invasive rod-shaped sensor in which the probe is retractable within the structure of the rod-shaped sensor, with the probe aligning flush with the inner surface of the exhaust pipe without protruding into the engine's airflow duct. This design protects the probe from erosion by the exhaust gas particles. It offers distinct advantages, including insensitivity to particle adhesion on the probe, minimal interference with the airflow field, and enhanced safety for the engine. Figure 2 illustrates the non-invasive electrostatic sensor structure (NESS). The sensor features a cylindrical nickel-based alloy probe, with high-temperature-resistant ceramic serving as an insulating layer between the probe and the shielding casing. The shielding casing is grounded to mitigate external electromagnetic interference. The nickel-based alloy ensures the probe maintains good conductivity even in extremely harsh, high-temperature operating environments. The insulating layer isolates the probe from the casing, preventing heat-induced damage to the sensor's internal components.

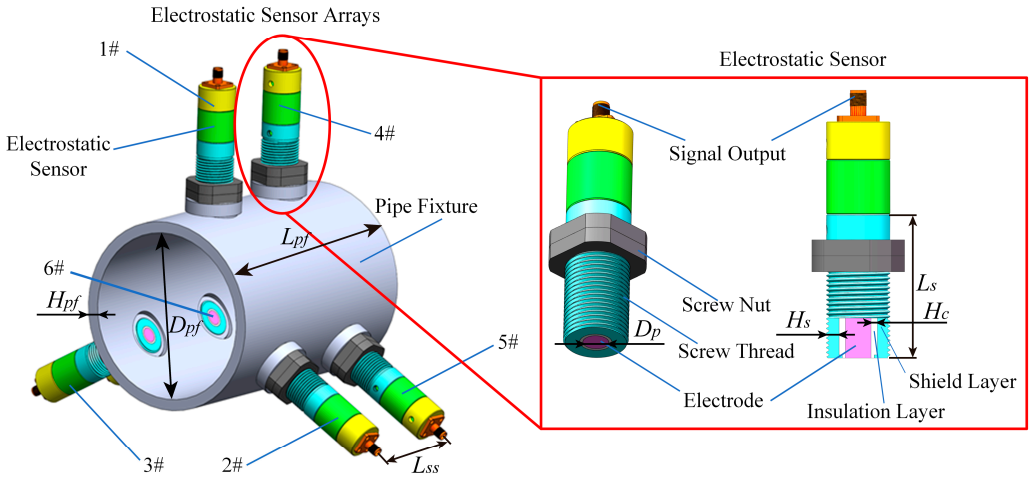


Figure 2. Physical structure of the electrostatic sensor, and the 1#, 2#, 3#, . . ., 6# represent sensor number.

The geometric parameters of the designed NESS assembly are shown in Table 1. In Table 1, L_{pf} represents the total length of the pipe fixture, D_{pf} is the inner diameter of the pipe fixture, H_{pf} is the wall thickness of the pipe fixture, L_{ss} is the center-to-center distance between two axial sensors, H_s is the equivalent thickness of the sensor shielding casing, L_s is the length of the sensor shielding casing, H_c is the equivalent thickness of the sensor insulation ceramic, and D_p is the diameter of the sensor probe.

Table 1. Geometric parameters of NESS.

L_{pf}/mm	D_{pf}/mm	H_{pf}/mm	L_{ss}/mm	H_s/mm	L_s/mm	H_c/mm	D_p/mm
140	90	6	60	4.5	45	2	8

2.5. Mathematical Model of the Non-Intrusive Electrostatic Sensor

Before formally exploring the electrostatic properties of the SiC/SiC particles in the engine exhaust, it is imperative to establish an adequate mathematical model of electrostatic induction and conduct a comprehensive theoretical analysis, thereby furnishing essential theoretical underpinnings for subsequent signal analyses. For this reason, a mathematical model for the sensor's induced electrostatic response is established to understand the interaction between charged particles in the engine exhaust and the electrostatic sensor.

The non-invasive rod-shaped probe is the crucial component of the electrostatic sensor for inducing charged particles. The probe primarily generates surface-induced charges on the flat end face of the cylindrical probe. Therefore, the modeling here focuses mainly on the induced characteristics of the charged particles on the flat end face. In the modeling process, the size of the charged particles is neglected, treating them as point charges with a charge of $+q$. Assuming the charged particles move along the Z-axis with a constant linear velocity, the variation in the position of the charged particles results in a change in the electric field distribution within the duct. According to the principles of electrostatic induction, the probe responds to the passage of the particles.

Figure 3 illustrates the electric field diagram generated by a particle with a charge of $+q$ when it passes through point P near the non-invasive electrostatic sensor probe. The electric field lines emitted by the charged particles are distributed across the probe's surface. According to the principles of electric field theory [38], it can be inferred that the electric field lines emitted by the particles are perpendicular to the probe's surface, representing the induced charge on the non-invasive electrostatic sensor.

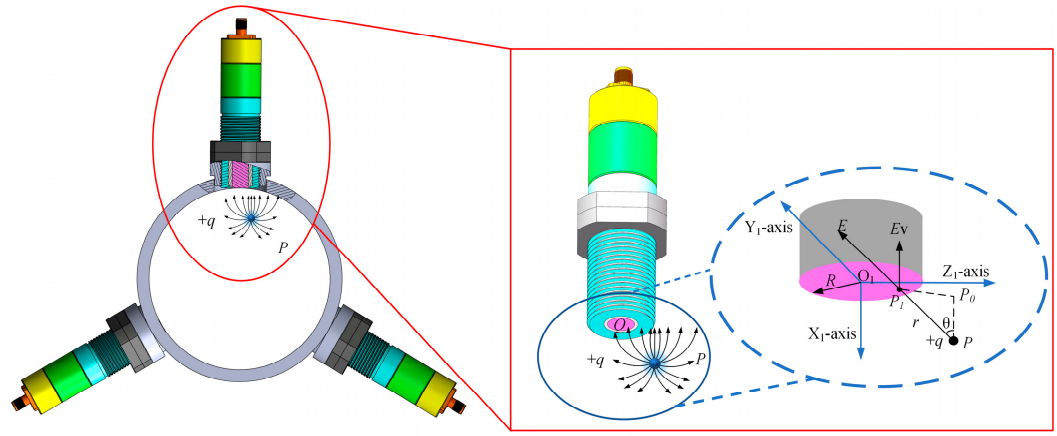


Figure 3. Schematic of the induced electric field by charged particles.

Now, a local Cartesian coordinate system $X_1Y_1Z_1$ is established, and its origin is at the center of the probe's flat end face, denoted as O_1. Assuming a point charge of $+q$ is located at spatial position P (x_1, y_1, z_1), the induced electric field at point P_1 (e, f, g) on the lower end face of the probe is depicted in Figure 3. Here, P_0 represents the projection of point P onto the probe's end face, E denotes the induced field strength at point P_1 on the lower end face, E_v is the projection of E in the vertical end face direction, θ represents the angle between E and E_v, R is the radius of the probe, and r is the distance between P and P_1. The induced charge, Q, produced by the probe in response to the $+q$ charge at point P is accounted for due to electrostatic induction.

The electric field strength E at the point P_1 is given by:

$$\boldsymbol{E} = \frac{q}{4\pi\varepsilon_0 r^2} = \frac{q}{4\pi\varepsilon_0\left[(x_1-e)^2+(y_1-f)^2+(z_1-g)^2\right]^2} \tag{3}$$

where E is the electric field strength at point P_1, ε_0 is the electric constant (permittivity of free space), q is the particle's charge, and r is the distance between the point charge at P and point P_1.

The electric field strength component E_v perpendicular to the end face can be calculated as follows:

$$E_v = E \cdot \cos\theta \tag{4}$$

where E_v is the electric field strength component perpendicular to the end face, and θ is the angle between the electric field E and the projection E_v.

The ultimate electric field strength E_v is determined as follows:

$$E_v = \frac{qx_1}{4\pi\varepsilon_0\left[(x_1-e)^2+(y_1-f)^2+(z_1-g)^2\right]^{3/2}} \tag{5}$$

According to Gauss's theorem, commonly employed in the electrostatic field, assuming the point area of P_1 is denoted as dS, the induced charge quantity at point P_1, represented as dQ, can be expressed as follows:

$$dQ = \varepsilon_0 E_v dS = \frac{qx_1}{4\pi\left[(x_1-e)^2+(y_1-f)^2+(z_1-g)^2\right]^{3/2}} dS \tag{6}$$

where dQ is the induced charge quantity at point P_1, and dS is the point area of P_1.

The total induced charge quantity Q across the entire end face can be obtained through integration as follows:

$$Q = \frac{qx_1}{4\pi}\iint_S \frac{1}{\left[(x_1-e)^2+(y_1-f)^2+(z_1-g)^2\right]^{3/2}} dS \tag{7}$$

Performing a polar coordinate transformation on the coordinates of point P_1 results in $e = 0$, $g = r \times \sin\theta$. Substituting this value into Equation (7), we obtain the final expression for Q:

$$Q = \frac{qx_1}{4\pi}\int_0^{2\pi} d\theta \int_0^{R} \frac{r}{\left[(x_1)^2+(y_1-r\cdot\cos\theta)^2+(z_1-r\cdot\sin\theta)^2\right]^{3/2}} dr \tag{8}$$

Through Equation (8), we can obtain the charge of the electrostatic sensor when the particle is at any position within space. It is evident that the total induced charge quantity in the electrostatic sensor is primarily influenced by three key factors: the charge value of the particles q, the radius of the probe's end face R, and the spatial position P of the point charge. Furthermore, the induced charge in the probe is positively correlated with the charge value of the particles q and the radius of the probe's end face R. At the same time, it is inversely related to the measured distance from the point charge at position P. During the moving process, the moving particles incessantly induce a charge on the probe, which forms a pulse waveform.

2.6. The Principle of Exhaust Gas Electrostatic Monitoring

In a healthy state, aero-engines typically have charged particles in their exhaust, primarily small-sized carbon soot particles with diameters falling within 5–7 nm and 20–40 nm. The overall electrostatic charge level in the exhaust remains relatively stable, and the variations primarily depend on the engine's operating conditions. However, many abnormal particles are generated when the engine's components degrade or experience malfunctions. These abnormal particles have larger diameters, typically exceeding 50 μm [39].

Changes in the engine operating conditions or malfunctions can alter parameters such as the temperature, particle concentration, gas velocity, or particle size distribution in the exhaust [40,41]. This, in turn, leads to variations in the overall electrostatic charge level

within the engine's gas path. These particles are in constant motion due to rapid flow, turbulence, vibration, and other factors. Consequently, they undergo contact, collision, and friction with and separation from other particles and the duct's inner walls. These interactions result in the accumulation of electric charges on the particles, leading to electrostatic phenomena [42]. When charged particles pass over the sensor's surface, they can induce an electrical current, converted into voltage by conditioning circuits. The magnitude of the induced voltage reflects the particle size, as it is related to the charge carried by the particles, and the charge's polarity reflects the particles' material properties. Figure 4 is a schematic of the engine exhaust gas electrostatic monitoring system.

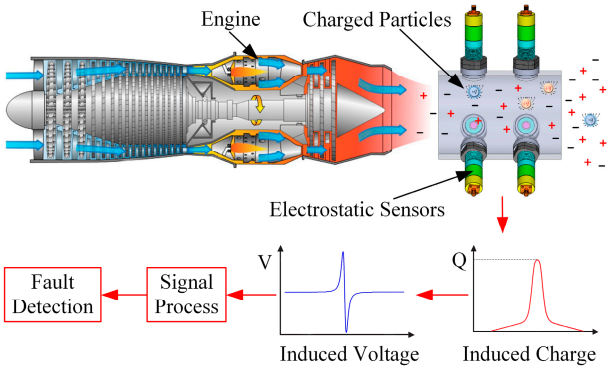


Figure 4. Schematic of the engine exhaust gas electrostatic monitoring system.

3. Experimental and Method

3.1. The Micro Turbine Engine Fault Simulation Test Stand

This section provides an experimental setup of a micro turbine engine to simulate faults in a real aero-engine. The focus of electrostatic monitoring lies in studying the abrasive particles generated by wear-type faults in the engine gas path. These particles are crucial in reflecting the specific fault characteristics of the gas path. To investigate the electrostatic properties of SiC/SiC abrasive particles under actual engine conditions, a J20-type micro turbojet engine electrostatic monitoring test bench is established. This equipment is manufactured by Changzhou Huanneng Turbo Power Co., Ltd., Changzhou, China. Figure 5 provides a schematic of the experimental system.

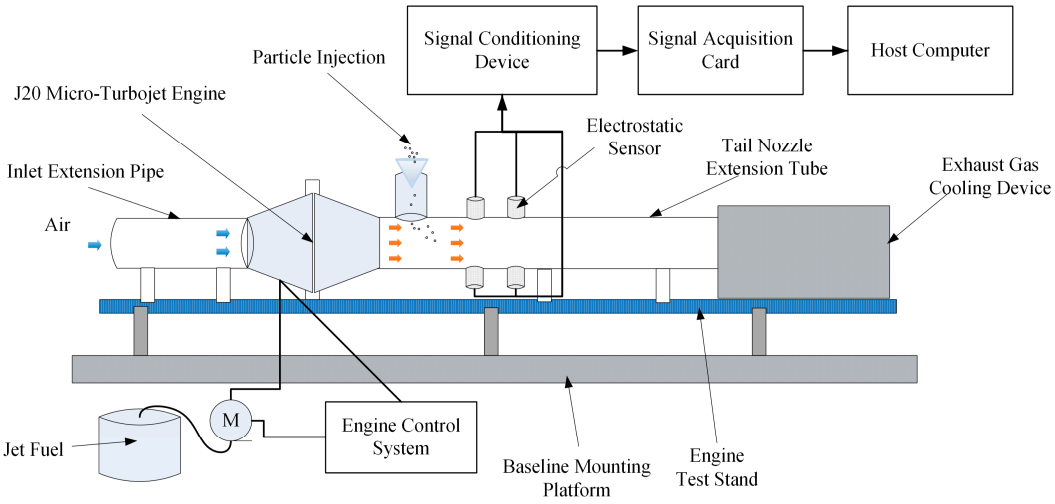


Figure 5. A schematic of the experimental system.

The fault simulation experiment platform system primarily comprises several components: (1) A J20-type micro-turbojet engine (a small turbojet engine with 20 kg of thrust)

and its control devices; (2) an inlet extension pipe; (3) a tail nozzle extension tube, particle injection equipment, and an exhaust gas cooling device; (4) an electrostatic signal acquisition system, including an electrostatic sensor, signal conditioning circuit, signal acquisition card, and host computer. Air passes through a sequence of components, including the inlet extension pipe, the small turbojet engine, the tail nozzle extension tube, and the exhaust gas cooling device. The particle injection device injects the test particles into the engine's exhaust duct during the experiment. They are then monitored for their electrostatic levels using the custom-designed, non-invasive electrostatic sensor located inside the extension tube of the tail nozzle. The injection point is approximately 10 cm from the electrostatic sensor. Figure 6 shows a physical representation of the experimental setup.

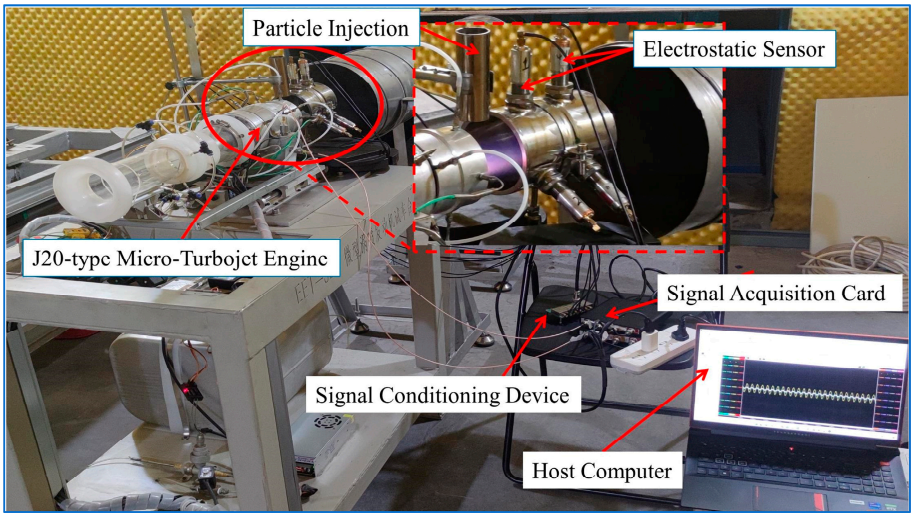


Figure 6. The physical representation of the experimental setup.

3.2. Experimental Methodology

In previous studies, researchers have classified the factors affecting the charge characteristics of exhaust particulate matter into exhaust gas material properties [31–33,43], temperature [33], particle mass concentration [43–46], particle size [33,43–46], and aero-engine exhaust gas velocity [43–46] according to the operating environment of the engine. This paper also uses the above factors to facilitate the comparison and analysis. Four distinct factors were considered to thoroughly investigate the electrostatic properties of SiC/SiC particles: temperature, mass concentration, size, and velocity. These situations can simulate different states of SiC/SiC particles produced by engines with various degrees of falling blocks and collision faults.

The experimental procedure is illustrated in Figure 7. First, a temperature comparison experiment is conducted. By maintaining the same mass concentration, particle size, and exhaust gas velocity, the impact of SiC/SiC particles on the characteristic parameters of the electrostatic sensor signal under low- and high-temperature (°C) conditions is studied and compared with different materials. Secondly, under high-temperature conditions, the effects of three variable conditions for SiC/SiC—particle mass (g), particle size (μm), and exhaust gas velocity (m/s)—on the characteristic parameters of the electrostatic sensor signal are investigated. Since the volume of the exhaust pipe is constant, the particle mass concentration is controlled by adjusting the mass of injected particles.

Following the principle of single-variable control experiments, the induction signals of the electrostatic sensor under different variable conditions are collected. The experimental data are obtained by performing ten trials for averaging. Finally, each set of signals is analyzed to obtain the characteristic parameters of the particle electrostatic signal under each variable condition and then compared for further insights.

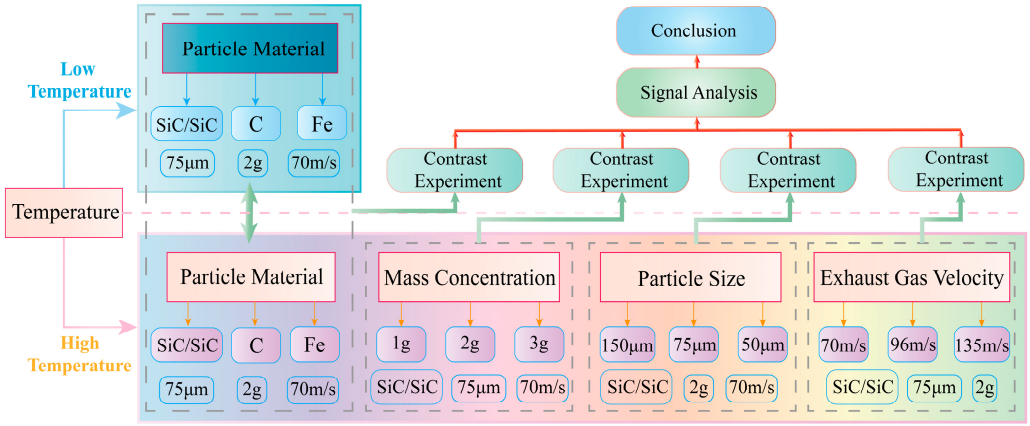


Figure 7. Process of experiment program.

3.3. Materials

As shown in Figure 8, the SiC/SiC material used in the experiments is a typical CMC. It was prepared using the Chemical Vapor Infiltration (CVI) process by the Shanghai Institute of Ceramics. Fe and C particles are also compared with the SiC/SiC particles. The reason is that they are typically three different materials because Fe is metallic, C is non-metallic, and SiC/SiC belongs to composite materials, respectively.

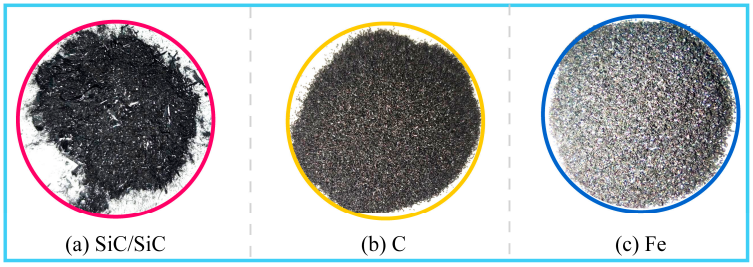


Figure 8. Three types of material particles used in the wear simulation experiments.

These material particles are classified into three specifications, each obtained by screening with two different mesh sizes of industrial screens. Assuming the screened particle sizes are uniformly distributed, the parameters for each specification are shown in Table 2. In Table 2, "Industrial Sieve Specification" refers to the two different industrial screen specifications used to screen the particles. "Particle Size Range" represents the range of particle sizes obtained through these screens. "Standard Deviation" is the estimated standard deviation of the screened particles. "Average Diameter" is the estimated average diameter of the screened particles. "Defined Particle Size" refers to the size determined from the estimated average diameter to facilitate discussion. For simplicity, we defined these sizes as 50 μm, 75 μm, and 150 μm.

Table 2. Parameters of particles in three specifications.

Industrial Screens (mesh)	Particle Size Range (μm)	Standard Deviation (μm)	Average Diameter (μm)	Defined Size (μm)
280, 300	48~53	1.44	50.50	50
180, 220	68~80	3.46	74.00	75
90, 100	150~165	4.33	157.5	150

To provide a comprehensive analytical characterization of the SiC/SiC particles used in the experiments, optical microscopy was conducted using a high-resolution microscope to capture detailed images of the particles. Figure 9 shows microscopic images of SiC/SiC particles with sizes of 50 μm, 75 μm, and 150 μm. The 50 μm and 75 μm particles were

imaged at 5× magnification, while the 150 µm particles were imaged at 5×, 20×, and 50× magnification. These images allowed us to analyze the particles' size distribution and surface features, which are critical for understanding their behavior in the high-temperature and high-speed environments typical of aero-engine exhaust systems.

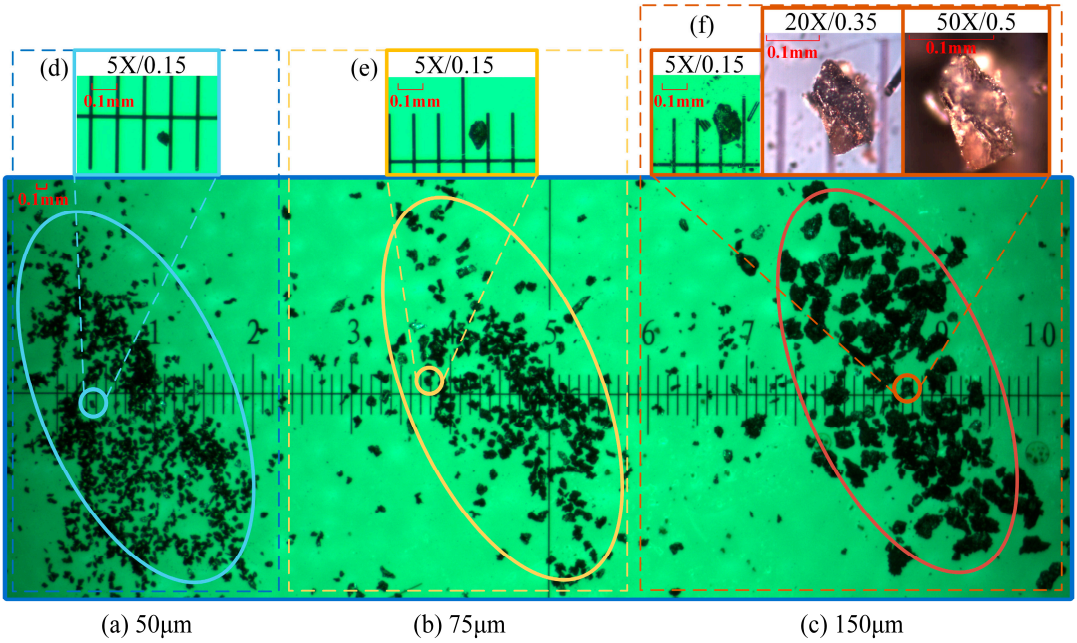


Figure 9. Microscopic images of SiC/SiC particles at different sizes: (**a**) 50 µm particles, (**b**) 75 µm particles, (**c**) 150 µm particles, (**d**) single 50 µm particle magnified 5 times, (**e**) single 75 µm particle magnified 5 times, (**f**) single 150 µm particle magnified 5 times, 20 times, and 50 times.

3.4. Data Acquisition

To suppress noise from the environment, the signals from the sensor electrodes are transmitted to the signal conditioning unit through coaxial cables. The electrical signals from the sensors are amplified and filtered by the signal conditioning unit. Subsequently, the signals are sampled using a data acquisition card and processed by the host computer. A block diagram of the measurement system is illustrated in Figure 10.

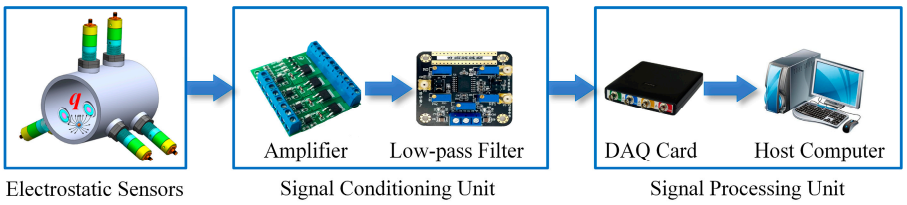


Figure 10. Block diagram of the measurement system.

3.5. Data Processing Methodology

3.5.1. Signal Processing Technology

The pulse signals generated by the charged particles passing through the sensor indirectly reflect the polarity of the charge and the magnitude of the particles. In practical applications, the signals collected from the electrostatic sensor often contain noise [47], DC components, and baseline drift [48], which can lead to the drowning of feeble proper signals by noise. Therefore, noise is a significant obstacle in electrostatic monitoring and diagnostic technology.

This paper adopts the following signal denoising process to extract the characteristics of electrostatic signals from particles and ensure the accuracy of SiC/SiC electrostatic analysis. First, the DC component from the signal is removed [49], and then the CEEMDAN [50]

method is employed to eliminate noise. Finally, data smoothing [51] is performed on the signal. Figure 11a displays the raw signals collected in this experiment, containing three simulated fault signals. However, the original signals are heavily contaminated with noise, with the second simulated fault signal nearly submerged by noise. Figure 11b shows the signals after processing and denoising using the abovementioned method. It is evident that this approach effectively filters out much of the noise, and the three simulated fault signals are now clearly visible. Therefore, this signal processing method successfully extracts the valuable components from the data.

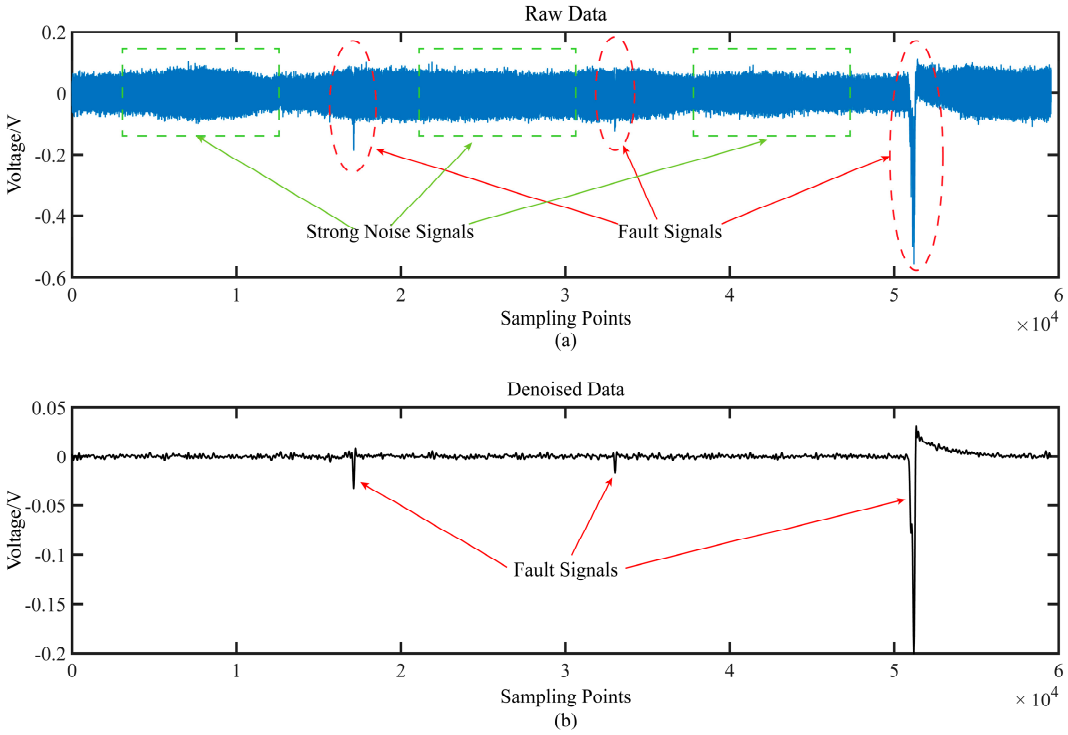


Figure 11. The raw data and the denoised data obtained through signal processing methodology: (**a**) The raw data; (**b**) The denoised data.

3.5.2. Feature Extraction

The previously described signal processing steps can effectively obtain valuable signals. However, in practical circumstances, analyzing the signals solely in the time domain may only partially characterize their electrostatic features. To obtain more useful features for improved discrimination, paper [47] and paper [17] proposed three indices that represent different electrostatic features: root mean square (RMS) or the standard deviation for mean zero, activity level (AL), and event rate (ER).

(1) Root Mean Square

The root mean square (RMS) value represents the energy measurement and relies on the total charge level of the exhaust gas and the exhaust velocity. The RMS value can be calculated as follows:

$$\mathrm{RMS}(t) = \sqrt{\frac{1}{N}\sum_{i=N\times(t-1)+1}^{N} C_f^2(i)} \tag{9}$$

where $C_f(i)$ represents the i th data point of the signal, and N is the total number of samples within a 1 s interval; an RMS value is computed for each second.

(2) Activity Level

The activity level (AL) is a metric that gauges the presence of high-frequency content, providing insight into the quantity of fine particles in the exhaust gas, such as carbon soot and other minute particulate matter [39]. The calculation for AL is as follows:

$$\mathrm{AL}(t) = \sqrt{\frac{1}{N}\sum_{i=N\times(t-1)+1}^{N} Q_f^2(i)} \tag{10}$$

where $Q_f(i)$ represents the i th sampling point of induced charge, which is derived from the integration of the sensor readings. The activity level (AL) can be understood as the total charge accumulated on the sensor's surface due to charged particles in the exhaust gas within a 1 s timeframe.

(3) Event Rate

The event rate (ER) is associated with the quantity of larger charged particles, including significant carbon particles and large particles originating from faults found in the exhaust gas per second. The calculation for ER is as follows:

$$\mathrm{ER}(t) = \frac{M}{N} \times 100\% \tag{11}$$

where M represents the number of samples within a 1 s interval for which $\left|Q_f(i)\right| \geqslant K$ AL, and the constant K is typically empirically determined based on experimental and statistical data, with the typical values being 3, 5, or 10. The event rate (ER) is expressed as a percentage, and the events are categorized into positive event rate (PER) and negative event rate (NER) based on the polarity of the induced charge.

3.5.3. Charge Determination

According to the electrostatic monitoring principles described above, the electrostatic sensor will induce an induced charge, resulting in an output voltage signal that resembles a sine wave under the ideal circumstances when a positively charged particle passes through the sensor's sensing surface. On the other hand, when a negatively charged particle passes through the sensor, the sensor system will output a voltage signal corresponding to a cosine wave. The simulated electrostatic induction signals are shown in Figure 12.

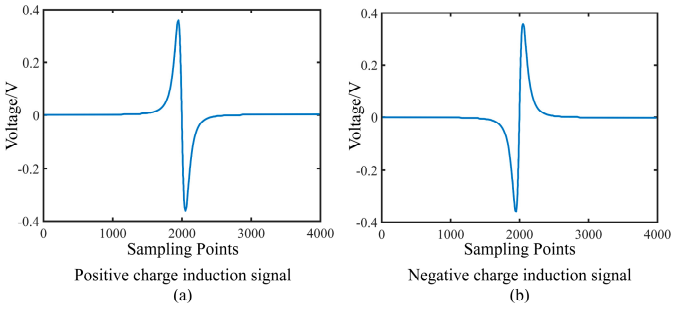


Figure 12. Electrostatic induction simulation signals: (**a**) positive charge induction signal, (**b**) negative charge induction signal.

However, during the actual engine testing, it was observed that the electrostatic sensor had hysteresis. When high-speed airflow from the engine passes through the sensor, the particle fault signal often appears as a positive pulse signal (for particles carrying a positive charge) or a negative pulse signal (for particles carrying a negative charge) [52], as shown in Figure 13. For the same input quantity, the input signal for the sensor's positive excursion (increasing input quantity) or negative excursion (decreasing input quantity) is not of equal magnitude, and this phenomenon is known as hysteresis. Therefore, we can use the sensor's hysteresis to monitor the electrostatic characteristics of the fault particles to

determine the particle polarity. When the positive amplitude of the signal is significantly greater than the negative amplitude, it can be concluded that the particle is positively charged. Otherwise, it is a negatively charged particle.

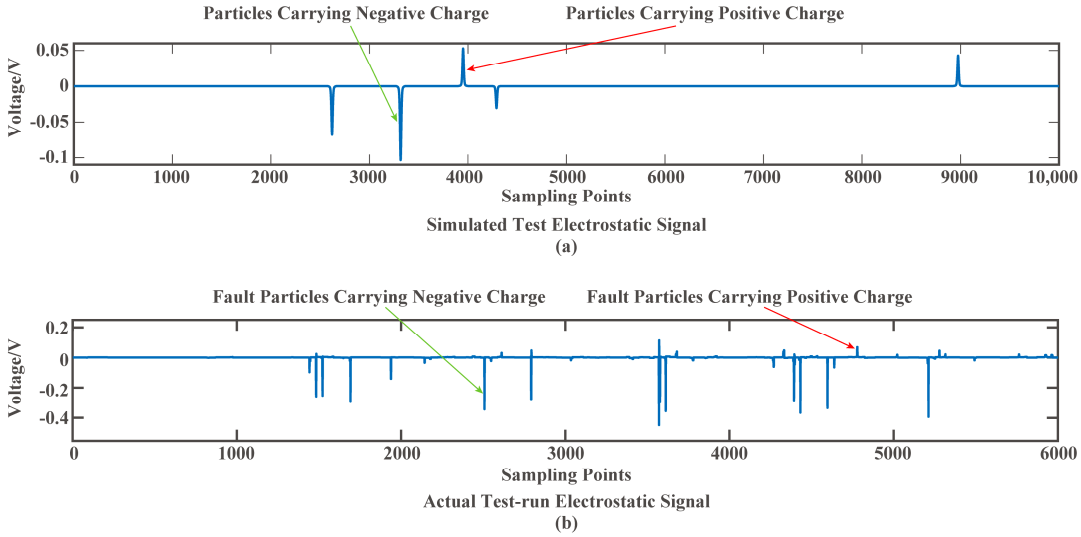


Figure 13. Hysteresis in electrostatic signals during aero-engine operation [52]: (**a**) simulated test electrostatic signal, (**b**) actual test-run electrostatic signal.

4. Results and Discussion

4.1. The Effect of Temperature on the Electrostatic Properties of SiC/SiC Particles

Since aero-engine testing typically involves both cold-start operating conditions and high-temperature combustion operating conditions after engine ignition, the experiments conducted in this paper are first divided into two categories: electrostatic characteristic experiments under the cold-start operating condition and electrostatic characteristic experiments under the high-temperature combustion operating condition.

The cold-start operating condition experiment procedure involves the engine not being ignited. The starter motor drives the engine's rotor to achieve a stable rotational speed of approximately 40,000 rpm while the temperature stabilizes at around 200 °C. Then, the particles are injected, and the electrostatic signals from these particles are collected. This constitutes the electrostatic characteristic experiment under the cold-start condition. Subsequently, the engine is driven by the starter motor to a speed of 10,000 rpm, and the engine is then ignited, further increasing the rotor speed to approximately 40,000 rpm. Then, the temperature remains stable at around 730 °C. Again, the particles are introduced, and their electrostatic signals are collected. For ease of reference, the following sections refer to the experiments conducted under cold-start conditions as the "low-temperature experiments" and those conducted under high-temperature combustion conditions as the "high-temperature experiments".

This section studies the electrostatic induction properties of charged SiC/SiC particles under low and high temperatures. Commonly charged particles found in engine exhaust, namely C and Fe, are used for comparison. In this experiment, the sizes of the particles are 75 μm, and when the speed of the aero-engine is about 40,000 rpm, the exhaust gas velocity of the aero-engine is about 70 m/s. Since the structure of the array sensor used in Figure 6 is symmetric, the signal trends collected by each sensor are similar. To avoid redundancy, the electrostatic induction signal presented in the following sections only shows the signal collected from Sensor 1, followed by the average value from the six sensors. The signals are displayed at 1 s intervals, and the electrostatic characteristics are calculated, namely RMS, PER, and NER, as mentioned in Section 3.5.2.

4.1.1. Low-Temperature Experiment

In the low-temperature experiment, SiC/SiC, C, and Fe particles with a mass of 2 g were sequentially injected into the engine's tail nozzle sample inlet. Figure 14a–d represent the denoised electrostatic signals, the RMS values of the electrostatic signals, the PER values, and the NER values, respectively. It can be observed that the three different particles' materials become charged through friction when driven by high-speed airflow, and the electrostatic sensor has significant signal variations. Notably, the voltage changes induced in the SiC/SiC, C, and Fe particles are at about 9 s, 16 s, and 24 s, respectively.

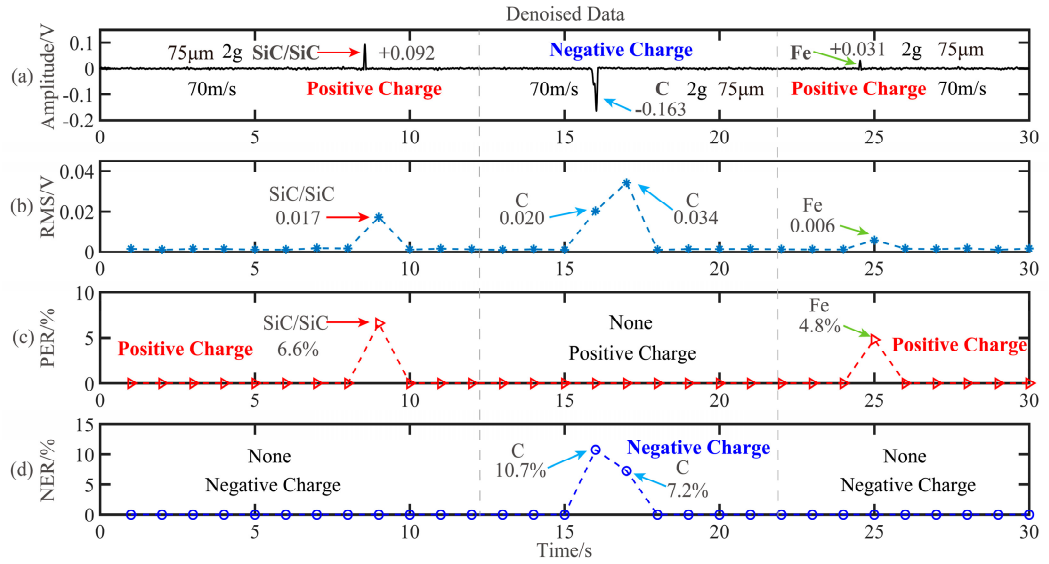


Figure 14. The induction signal from Sensor 1 and its characteristic parameters in the low-temperature experiment with particle sizes of 75 μm and 2 g: (**a**) the denoised electrostatic signals, (**b**) RMS of the fault signals, (**c**) PER of the fault signals, (**d**) NER of the fault signals.

The polarity of the induced voltage resulting from the friction of different materials with air is analyzed first. We can see from Figure 14 that both SiC/SiC and Fe abrasive particles, after the friction, initially lead to an increase in the induced voltage to positive values, followed by a subsequent decrease and finally a return to the background signal level. The PER and NER for SiC/SiC are 6.6% and 0, while for Fe, they are 4.8% and 0. This indicates that under low-temperature experimental conditions, SiC/SiC and Fe particles carry a positive charge after friction with air. In contrast, C abrasive particles cause the induced voltage to decrease and then increase and, after oscillation, return to the background signal level. Around 16 s, C exhibits PER values of 10.7% and 7.2%, with NER consistently at 0, indicating that C abrasive particles carry a negative charge after friction with air.

Then, the amplitudes of the electrostatic charge generated by friction are studied. The SiC/SiC has an intermediate value with a peak-induced voltage of 0.092 V. The Fe particles show the smallest induced voltage amplitude, with a peak value of 0.031 V. The C particles demonstrate the largest induced voltage amplitude, with a peak value of 0.163 V. As an energy indicator, the RMS value exhibits trends similar to those of the peak value. Figure 15 represents the array sensors' overall performance (the six sensors' mean values in Figure 6). The laws are the same as those of Sensor 1 alone.

The results indicate that the SiC/SiC (composite material), Fe (metal), and C (non-metal) particles with the same mass all become charged through friction at low temperatures. The SiC/SiC and Fe particles carry positive charge, while the C particles carry negative charge, and the C particles exhibit the highest charge magnitude.

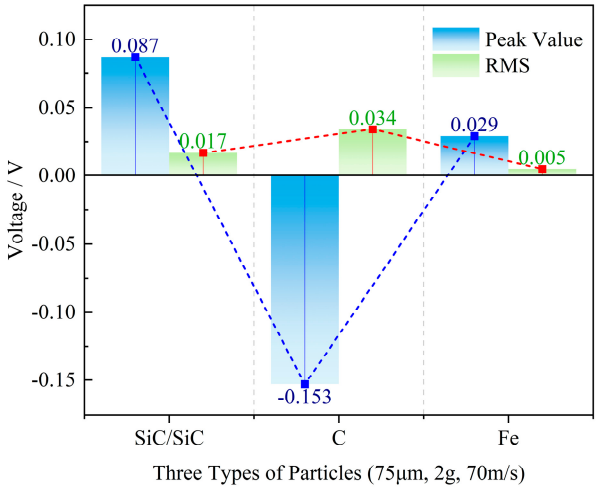


Figure 15. Under low-temperature conditions, different materials' peak values, RMS, and polarity indices (average of six sensors).

4.1.2. High-Temperature Experiment

Similarly, in the high-temperature experiment, particles of SiC/SiC, C, and Fe with a mass of 2 g were successively injected at the particle injection port. The electrostatic induction signals are illustrated in Figure 16. It can be observed that the three materials caused significant signal variations as they passed through the electrostatic sensor. Notably, the induced voltage changes in the SiC/SiC, C, and Fe particles occur at about 6 s, 12 s, and 17 s, respectively.

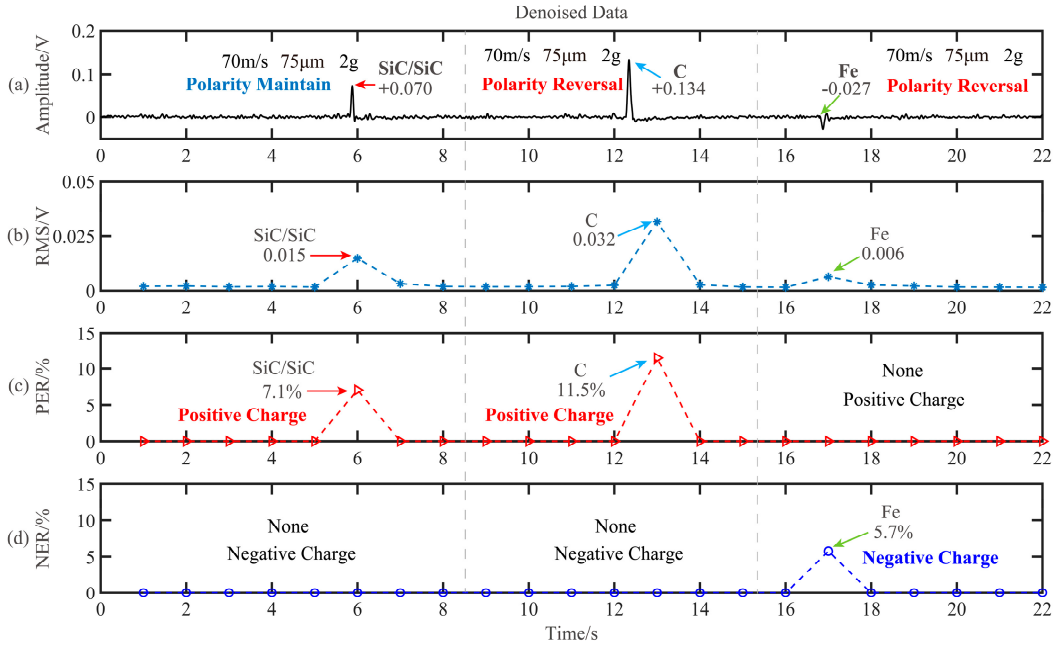


Figure 16. The induction signal from Sensor 1 and the characteristic parameters of the high-temperature experiment with particle sizes if 75 μm and 2 g: (**a**) the denoised electrostatic signals, (**b**) RMS of the fault signals, (**c**) PER of the fault signals, (**d**) NER of the fault signals.

The polarity of the induced voltage is analyzed first. The SiC/SiC and C particles initially caused the induction voltage to rise positively, followed by a subsequent decrease, eventually affecting the background signal level. The PER and NER for SiC/SiC are 7.1% and 0, while C exhibited PER and NER values of 11.5% and 0. This suggests that the SiC/SiC and C particles carry positive charges after passing through the engine nozzle

under high-temperature experimental conditions. In contrast, the Fe particles induced a voltage drop, followed by an increase, oscillating briefly before returning to the background signal level. The PER and NER for the Fe particles were 0 and 5.7%, indicating that the C particles became positively charged and the Fe particles acquired a negative charge due to friction with air after high-temperature combustion. The electrification characteristics of these three particles undergo intriguing changes after passing through the high-temperature engine burn. The SiC/SiC particles always maintain a positive charge polarity, whereas the C and Fe particles experience a reversal in their electrification polarity. C became positively charged, while Fe became negatively charged. The particle electrification characteristics are crucial for engine fault localization, and this is a significant finding in the present study, as this phenomenon has yet to be publicly reported in previous research.

The exact reasons for this phenomenon have yet to be conclusively determined. Based on our current understanding, it is likely that SiC/SiC, being a high-temperature-resistant composite material, remained stable in performance and did not undergo chemical reactions at the high temperature of 730 °C, thus consistent with the results from the previous low-temperature experiments. However, C and Fe experienced oxidation and ionization reactions in this high-temperature environment, leading to a noticeable change in the electrification characteristics of these materials. Since the electrification polarity of particles is related to their ability to gain or lose electrons, it can be inferred from the above study that SiC/SiC particles have a solid electron-losing ability, making them prone to carrying a positive charge through friction in the airflow. Therefore, the positive event rate of SiC/SiC particles could be a fault characteristic of engine SiC/SiC components in fault diagnosis. At the same time, this research conclusion holds significant engineering value for the initial localization of chunking-type faults that occur during an engine's cold- and high-temperature operations.

Regarding the amplitude of frictional electrification, the SiC/SiC particles still fall between C and Fe. The peak value of the induced voltage for the SiC/SiC particles is 0.070 V, while the peak value for the Fe particles is the smallest, at 0.027 V. The C particles exhibited the largest induced voltage amplitude, with a peak value of 0.134 V. The trend in the RMS values aligns with the peak values, reflecting similar behavior.

Figure 17 represents the overall performance of all six sensors (the average of the six sensors). The comparative experimental data on particles of different materials under high-temperature engine conditions make it evident that at the same mass, SiC/SiC and C particles in a high-temperature, high-speed airflow acquire positive charges. At the same time, Fe becomes negatively charged, with C having the highest charge.

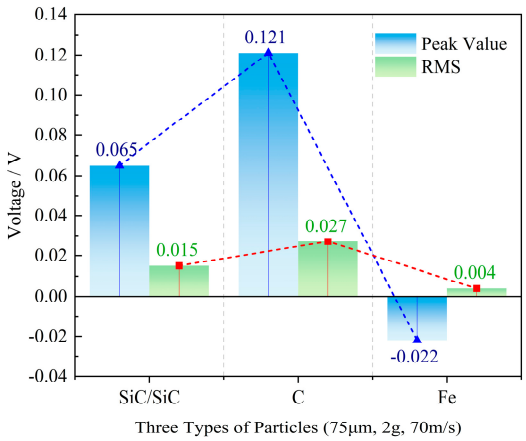


Figure 17. Under high-temperature conditions, different materials' peak values, RMS, and polarity indices (average of six sensors).

Comparing the results under low-temperature conditions, another significant change is that the amplitude of the induced voltage caused by the particles has decreased. The result represents that combustion has an essential effect on particles' electrostatic induction signal.

4.2. The Effect of Mass Concentrations on the Electrostatic Properties of SiC/SiC Particles

In addition to particle composition differences, particle mass concentration variations can result from wear on engine gas path components. These differences in concentration are typically related to the severity of wear. For example, minor rubbing between the blades and the casing may generate only a small number of particles. In contrast, continuous rubbing over an extended period could produce a significant number of particles. This section focuses on comparative experiments with varying mass concentrations of SiC/SiC material particles to address this issue. Because high-temperature conditions represent a typical operating scenario for engines, where engine rubbing faults are more likely to occur, monitoring results under high-temperature conditions are therefore presented.

Here, we use different masses to evaluate the effect of the mass concentrations. Due to the high-temperature, high-speed, and harsh working environment of aero-engine exhaust, the current aero-engine electrostatic monitoring test rigs are unable to accurately measure the concentration of injected fault particles. In the field of aero-engine electrostatic monitoring, except for some studies using ANSYS (version 2019 R1) simulation software to provide specific mass concentrations in simulated experiments [44–46], other experiments have been unable to provide accurate particle concentrations. In real aero-engine electrostatic monitoring tests, the common approach is to specify the mass of the injected particles [31–34,43], as ensuring the same particle mass in comparative tests can approximately guarantee the same mass concentration. Because the volume of the engine exhaust pipe is fixed, adding a fixed mass of particles can simulate conditions of the same mass concentration. Therefore, our experiments followed a similar method, injecting a fixed mass of particles in each comparative experiment to ensure a consistent particle mass concentration.

Similar to Section 4.1.2, at an engine speed of 40,000 rpm (with an exhaust velocity of approximately 70 m/s), we injected SiC/SiC particles with a particle size of 75 μm at masses of 1 g, 2 g, and 3 g and collected the corresponding electrostatic signals. The results of the electrostatic induction signals for the particles are shown in Figure 18. It can be observed that the peak values corresponding to 1 g, 2 g, and 3 g of the SiC/SiC particles were 0.052 V, 0.077 V, and 0.102 V, respectively. The corresponding RMS values were 0.011 V, 0.016 V, and 0.022 V, and the corresponding PER values were 6.6%, 7.6%, and 9.5%. The change in amplitude of the induced voltage still indicates that SiC/SiC particles carry a positive charge after friction with the airflow. Moreover, the induced voltage's amplitude gradually increases as the particle concentration increases. The reason is that as the particle concentration increases, the number of particles also increases. This leads to a higher probability of friction between particles and the pipe wall within a unit of time and space. With an increasing number of particles, the number of particles becoming charged due to friction with the air also increases. These factors contribute to an overall increase in the charge carried by the particle clusters. Therefore, the amount of electrostatic charge collected increases with the concentration of particles.

The experimental results indicate that SiC/SiC abrasion particles with different concentrations generate induced electrostatic charges when they pass through the engine nozzle jet stream. These particles exhibit a positive charge polarity, and the induced electrostatic voltage values increase with enhancement of the particle concentration, along with a corresponding increase in the event rates.

Figure 19 represents the overall performance of all six sensors (the average of the six sensors). The comparative experimental data on particles at different masses make it evident that at the same temperature, size, and velocity, the greater the mass concentration, the higher the charge of the SiC/SiC particles.

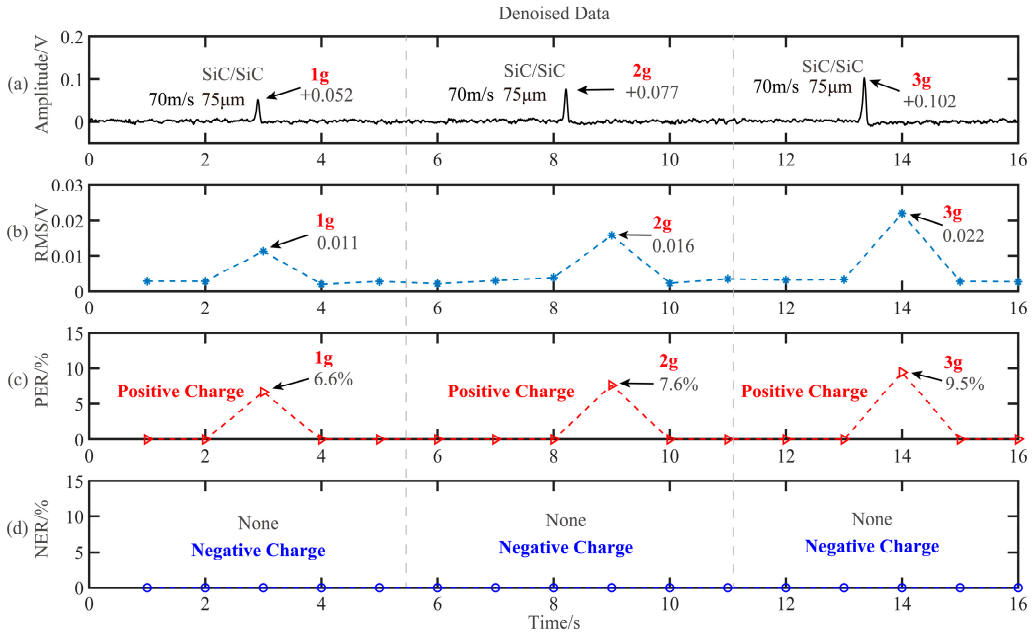


Figure 18. The induction signal from Sensor 1 and the characteristic parameters of different mass concentrations with particle sizes of 75 μm: (**a**) the denoised electrostatic signals, (**b**) RMS of the fault signals, (**c**) PER of the fault signals, (**d**) NER of the fault signals.

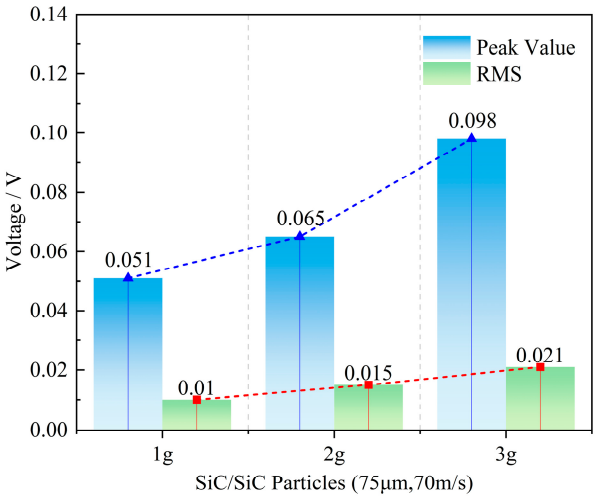


Figure 19. Comparison of electrostatic parameters for 75 μm SiC/SiC particles at different mass concentrations: peak values, RMS, and polarity indices (average of six sensors).

4.3. The Effect of Sizes on the Electrostatic Properties of SiC/SiC Particles

The particles generated by engine gas path component faults typically have a diameter of 40 μm or significantly more [39]. The particle size is related to the type of fault. For instance, the particles generated by erosive and abrasive wear tend to be at the micrometer level in size, while particles resulting from surface material peeling can reach millimeters in size or even significantly more. Therefore, experiments were conducted with three particle sizes greater than 40 μm. The particle size experiments were also carried out under high-temperature conditions at an engine speed of 40,000 rpm (with an exhaust velocity of approximately 70 m/s). Particles with diameters of 150 μm, 75 μm, and 50 μm were introduced with a mass of 2 g separately. Based on the particle size parameters provided in Section 3.3, the number of particles for a 2 g sample is approximately 3.04×10^4, 2.94×10^6, and 9.61×10^6 for the respective sizes. The resulting electrostatic induction signals for the SiC/SiC particles are shown in Figure 20.

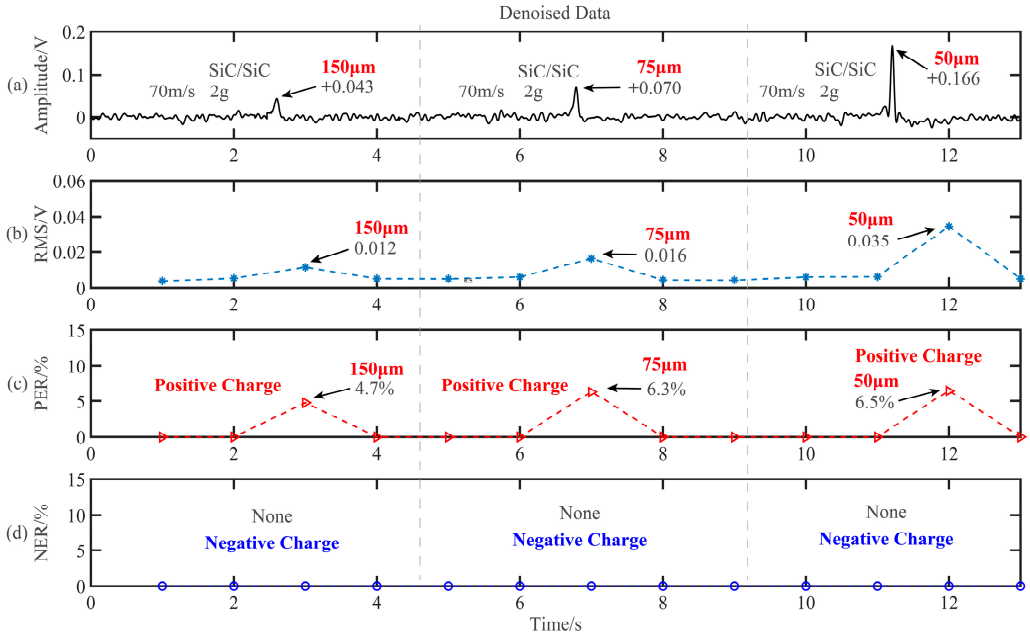


Figure 20. The induction signal from Sensor 1 and the characteristic parameters of different particle sizes: (**a**) the denoised electrostatic signals, (**b**) RMS of the fault signals, (**c**) PER of the fault signals, (**d**) NER of the fault signals.

It can be observed that the peak values of the SiC/SiC abrasion particles corresponding to 150 μm, 75 μm, and 50 μm were 0.043 V, 0.070 V, and 0.166 V, respectively. The corresponding RMS values were 0.012 V, 0.016 V, and 0.035 V, and the corresponding PER values were 4.7%, 6.3%, and 6.5%. The change in the amplitude of the induced voltage still indicates that SiC/SiC particles carry a positive charge after friction with the airflow. Moreover, as the particle diameter decreases, the amplitude of the induced voltage shows a clear trend of a gradual increase. Additionally, it was found that with a decrease in the particle size, the ratio of the corresponding event rates also increased.

This phenomenon can be attributed to three primary factors: First, under the same mass conditions, as the particle diameter decreases, the number of particles increases, leading to a higher probability and quantity of friction between particles and the pipe wall within a unit of time and space. Second, with an increase in the number of particles, the particles become charged due to friction with the air, resulting in an overall increase in the charge carried by the particle clusters. Since the monitored electrostatic charge is collected in the form of these particle clusters via the electrostatic sensor, the amount of electrostatic charge collected increases with the particle concentration. Third, as the particle diameter decreases, the particles experience more intense turbulence in the airflow, resulting in more thorough friction with the air. Therefore, the smaller the particle size, the greater the overall charge carried by the particle clusters.

The experimental results demonstrate that SiC/SiC abrasion particles with different sizes can all generate induced electrostatic charges when they pass through the engine nozzle jet stream. These particles exhibit a positive charge polarity, and the induced electrostatic voltage values increase as the particle size decreases, along with a corresponding increase in event rates.

Figure 21 represents the overall performance of all six sensors (the average of the six sensors). The comparative experimental data on particles of different sizes show that with the same temperature, mass concentrations, and velocity, the smaller the particle size, the greater the charge of the SiC/SiC particles within the size range of 50 μm to 150 μm.

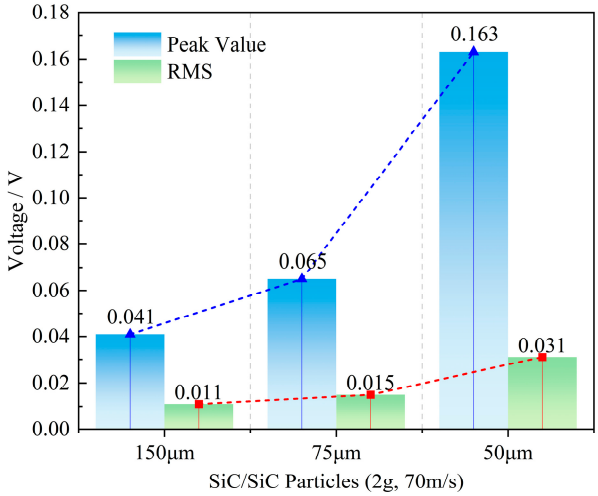


Figure 21. Comparison of electrostatic parameters for SiC/SiC particles of different sizes: peak values, RMS, and polarity indices (average of six sensors).

This is the opposite conclusion to the previous study [33], which suggested that the larger the particles, the greater the electrical signals, and a possible reason for this is that engine fault particles typically appear in clusters. Smaller particle clusters experience more intense friction with the air and the engine casing wall, resulting in a more significant charge. It is worth noting that the conclusion in reference [33], which states that larger particles carry a more significant charge, was based on experiments with large metal screws (1 mm). Due to the limitations of our test rig, we could not introduce such large particles, as they would damage the exhaust collection channel. Therefore, the largest particle size in our experiment was limited to 150 μm, and we did not attempt to test particles of a larger magnitude, which will be a direction of future research.

4.4. The Effect of Velocity on the Electrostatic Properties of SiC/SiC Particles

Under different operational states, such as takeoff, landing, and cruising, the power of the aero-engine changes, leading to significant variations in the exhaust gas velocity. Consequently, the charge carried by particles in the exhaust gas also varies. Therefore, this section conducts a comparative experiment on the electrostatic signals of SiC/SiC particles at different exhaust gas velocities in the engine, analyzing the characteristics of their induction signals and signal parameters.

In this set of experiments, the initial conditions were as follows: a particle size of 75 μm and a particle mass of 2 g, with the variable condition being the exhaust gas velocity of the aero-engine. After starting and igniting the aero-engine, the engine speed was controlled to operate at 40,000 rpm, 60,000 rpm, and 80,000 rpm, corresponding to three typical operating conditions of the micro turbojet engine: low-power, medium-power, and high-power states. Data were collected 10 s before and after the injection of SiC/SiC particles at each speed to calculate the exhaust gas velocity, yielding average airflow speeds of approximately 70 m/s, 96 m/s, and 135 m/s, respectively.

Under these three different engine speeds, the SiC/SiC particles were injected into the intake port of the device according to the experimental procedure. Data were collected during different airflow velocity stages to obtain various electrostatic induction signals. The signal analysis is shown in Figure 22, where the time intervals are as follows: 0–10 s for an engine speed of 40,000 rpm (70 m/s airflow velocity), 11–20 s for an engine speed of 60,000 rpm (96 m/s airflow velocity), and 21–29 s for an engine speed of 80,000 rpm (135 m/s airflow velocity).

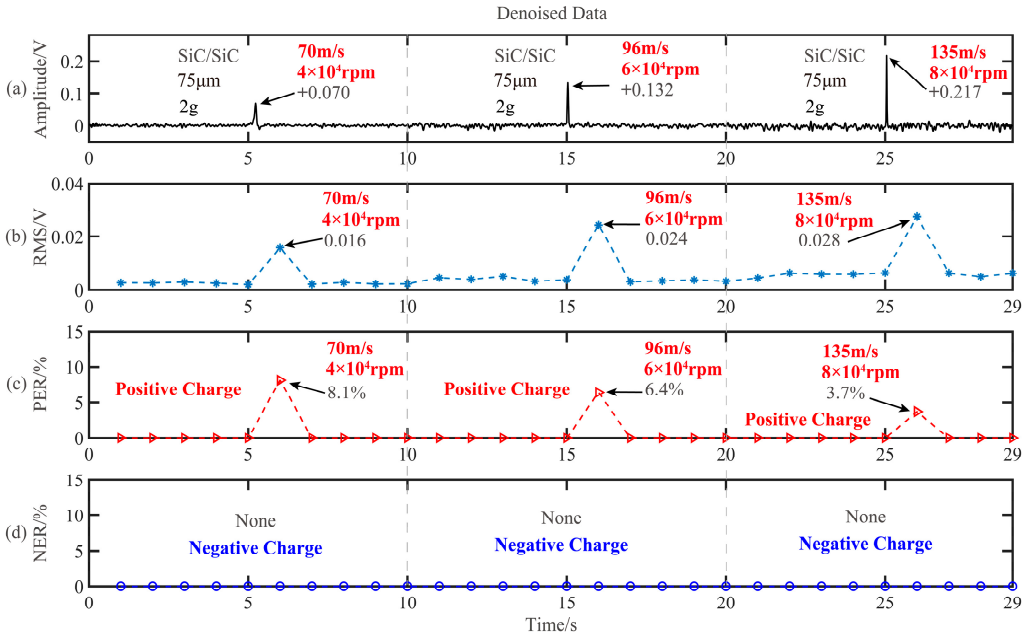


Figure 22. The induction signal from Sensor 1 and the characteristic parameters of different exhaust gas velocities: (**a**) the denoised electrostatic signals, (**b**) RMS of the fault signals, (**c**) PER of the fault signals, (**d**) NER of the fault signals.

Figure 22a shows the electrostatic time-series signals of the SiC/SiC particles at different engine speeds after noise reduction. Figure 22b–d display the corresponding RMS, PER, and NER parameters, respectively. The analysis results indicate that the SiC/SiC particles become charged due to friction with the pipe walls or airflow under the influence of the engine exhaust, causing significant fluctuations in the electrostatic sensor signal amplitude. It was observed that the amplitude of the induction signal increases with the exhaust gas velocity. This is likely because higher gas velocities increase the collision intensity of particles with the pipe walls and accelerate the separation process, leading to an increase in the charge of the SiC/SiC particles.

In Figure 22a, the peak parameters maintain different value ranges at various exhaust gas velocities. It is evident that the electrostatic values increase significantly at higher velocities, with corresponding peak values of 0.070 V, 0.130 V, and 0.217 V. In Figure 22b, the corresponding RMS values are 0.016 V, 0.024 V, and 0.028 V. In Figure 22c, the corresponding PER values are 8.5%, 6.4%, and 3.7%. Additionally, Figure 22d shows that the NER values are consistently 0, indicating that the SiC/SiC particles remained positively charged throughout the experiments.

Figure 23 represents the overall performance of all six sensors (the average of the six sensors). The comparative experimental data on particles at different exhaust gas velocities show that as the exhaust gas velocity increases, the continuous induction signal of the particles also strengthens. The conclusion is that higher exhaust gas velocities result in greater induced voltage amplitudes and higher RMS parameters for the SiC/SiC particles. Notably, as the gas velocity increases, there is a slight decreasing trend in the PER parameter. This is because the ER calculation is based on weighted data per second. When engine fault particles pass through the exhaust nozzle, they flow in clusters. With increased gas velocity, the speed of these particle clusters increases, leading to a higher peak charge but a reduced number of clusters detected per unit time compared to at lower velocities.

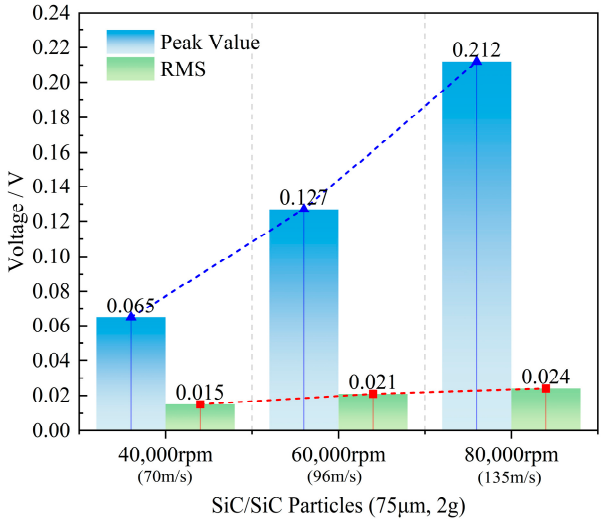


Figure 23. Comparison of electrostatic parameters for SiC/SiC particles at different exhaust gas velocities: peak values, RMS, and polarity indices (average of six sensors).

5. Conclusions

Failure monitoring of aero-engine SiC/SiC components is extremely important. This paper proposes a novel electrostatic monitoring method to examine this new material in exhaust gases. The factors affecting the electrostatic level of SiC/SiC are analyzed, and failure simulation experiments are carried out on a J20 turbojet engine experimental platform. The research concludes with the following findings:

1. Under cold operational conditions, SiC/SiC (composite material) particles and Fe (metal) particles acquire a positive charge after friction with the airflow. In contrast, C (non-metallic) particles acquire a negative charge. Under high-temperature combustion conditions, the SiC/SiC particles maintain a positive charge even after exposure to high-temperature combustion and friction with the airflow. In contrast, the C and Fe particles experience a reversal in their electrostatic polarity. The C particles carry a positive charge, while the Fe particles carry a negative charge. At the same time, the high-temperature combustion reduces the induced voltage amplitude of the particles. Therefore, the emergence of the positive event rate can be a crucial characteristic feature for detecting faults in SiC/SiC components during engine fault monitoring.
2. Under the same airflow speed, temperature, and particle size, the greater the mass concentration of the SiC/SiC particles, the larger the amplitude of the voltage induced in the sensor, along with a higher PER parameter value. Under the same airflow speed, temperature, and mass concentration, SiC/SiC particles of smaller sizes have larger electrostatic induction amplitudes and PER parameter values within the size range of 50 μm to 150 μm. Under the same mass concentration and particle size, the greater the exhaust gas velocity, the larger the amplitude of voltage induced in the sensor, along with a lower PER parameter value.

The disadvantage of this research is that the particles are artificially injected. In the future, a turbine rotor made of SiC/SiC material will be constructed to verify the engine's falling blocks and collision failure realistically. This cannot be achieved at this time due to its expensive cost. However, the research in this paper has demonstrated the feasibility of utilizing electrostatic sensors to monitor SiC/SiC materials. This study lays the foundation for applying electrostatic sensors in the condition monitoring and failure diagnosis of engine components made from SiC/SiC materials.

Author Contributions: Conceptualization, Y.L. and H.Z.; methodology, Y.L. and Z.L.; software, Y.L., F.B., Z.G. and X.L.; validation, H.Z.; writing—original draft preparation, Y.L.; writing—review and

editing, Y.L. and Z.L.; supervision, H.Z. All authors have read and agreed to the published version of the manuscript.

Funding: This research was funded by the National Natural Science Foundation of China (U2133202 and U1933202), the Postgraduate Research and Practice Innovation Program of Jiangsu Province (KYCX22_0375), the Nanjing University of Aeronautics and Astronautics Ph.D. short-term visiting scholar project (ZDGB2022006), and the Interdisciplinary Innovation Fund for Doctoral Students of Nanjing University of Aeronautics and Astronautics (KXKCXJJ202205).

Data Availability Statement: The original contributions presented in the study are included in the article, further inquiries can be directed to the corresponding authors.

Acknowledgments: We sincerely thank Jing Cai from the Civil Aviation College of Nanjing University of Aeronautics and Astronautics for the support and funding provided for the aero-engine experiment in this paper. Special thanks to Jaspreet S. Dhupia from the Department of Mechanical and Mechatronics Engineering at the University of Auckland, New Zealand, for his guidance and assistance in writing this paper. We also extend our gratitude to Jaspreet S. Dhupia for his academic guidance and support to Yan Liu and Zhenzhen Liu during their visiting scholar period at the University of Auckland, which contributed significantly to the success of our collaboration.

Conflicts of Interest: The authors declare no conflicts of interest.

References

1. An, Q.; Chen, J.; Ming, W.; Chen, M. Machining of SiC ceramic matrix composites: A review. *Chin. J. Aeronaut.* **2021**, *34*, 540–567. [CrossRef]
2. Lin, H.; Zhou, M.; Wang, H.; Bai, S. Investigation of Cutting Force and the Material Removal Mechanism in the Ultrasonic Vibration-Assisted Scratching of 2D-SiCf/SiC Composites. *Micromachines* **2023**, *14*, 1350. [CrossRef] [PubMed]
3. Xu, M.; Girish, Y.R.; Rakesh, K.P.; Wu, P.; Manukumar, H.M.; Byrappa, S.M.; Udayabhanu; Byrappa, K. Recent advances and challenges in silicon carbide (SiC) ceramic nanoarchitectures and their applications. *Mater. Today Commun.* **2021**, *28*, 102533. [CrossRef]
4. Parveez, B.; Kittur, M.I.; Badruddin, I.A.; Kamangar, S.; Hussien, M.; Umarfarooq, M.A. Scientific Advancements in Composite Materials for Aircraft Applications: A Review. *Polymers* **2022**, *14*, 5007. [CrossRef]
5. Katoh, Y.; Snead, L.L.; Henager, C.H.; Nozawa, T.; Hinoki, T.; Iveković, A.; Novak, S.; Gonzalez de Vicente, S.M. Current status and recent research achievements in SiC/SiC composites. *J. Nucl. Mater.* **2014**, *455*, 387–397. [CrossRef]
6. Ohnabe, H.; Masaki, S.; Onozuka, M.; Miyahara, K.; Sasa, T. Potential application of ceramic matrix composites to aero-engine components. *Compos. Part A Appl. Sci. Manuf.* **1999**, *30*, 489–496. [CrossRef]
7. Wang, Y.; Zhang, G.; Zhang, X.; Yang, Q.; Yang, L.; Yang, R. Advances in SiC fiber reinforced titanium matrix composites. *Acta Met. Sin* **2016**, *52*, 1153–1170. [CrossRef]
8. Yu, F.-m.; Okabe, Y. Regenerated Fiber Bragg Grating Sensing System for Ultrasonic Detection in a 900 °C Environment. *J. Nondestruct. Eval. Diagn. Progn. Eng. Syst.* **2019**, *2*, 011006–011006-011008. [CrossRef]
9. El Rassi, J.; Hegeman, A.L.; Morscher, G.N. A ply-level electrical resistance approach to monitor crack evolution in a laminate SiC/SiC composites. *J. Eur. Ceram. Soc.* **2022**, *42*, 5355–5365. [CrossRef]
10. Godin, N.; Reynaud, P.; R'Mili, M.; Fantozzi, G. Identification of a Critical Time with Acoustic Emission Monitoring during Static Fatigue Tests on Ceramic Matrix Composites: Towards Lifetime Prediction. *Appl. Sci.* **2016**, *6*, 43. [CrossRef]
11. Rath, N.; Mishra, R.K.; Kushari, A. Aero engine health monitoring, diagnostics and prognostics for condition-based maintenance: An overview. *Int. J. Turbo Jet-Engines* **2022**, *40*, s279–s292. [CrossRef]
12. Chen, Z.; Zi, Y.; Xiao, Z.; Wang, Y.; Qing, S. A Bilateral Second-Order Synchrosqueezing Transform and Application to Vibration Monitoring of Aerospace Engine. *IEEE Trans. Instrum. Meas.* **2021**, *70*, 3517215. [CrossRef]
13. Tahan, M.; Tsoutsanis, E.; Muhammad, M.; Abdul Karim, Z.A. Performance-based health monitoring, diagnostics and prognostics for condition-based maintenance of gas turbines: A review. *Appl. Energy* **2017**, *198*, 122–144. [CrossRef]
14. Carter, T.J. Common failures in gas turbine blades. *Eng. Fail. Anal.* **2005**, *12*, 237–247. [CrossRef]
15. Yin, Y.; Wen, Z.; Guo, X. A novel method of Gas-Path health assessment based on exhaust electrostatic signal and performance parameters. *Measurement* **2024**, *224*, 113810. [CrossRef]
16. Wen, Z.; Hou, J.; Atkin, J. A review of electrostatic monitoring technology: The state of the art and future research directions. *Prog. Aerosp. Sci.* **2017**, *94*, 1–11. [CrossRef]
17. Sun, J.; Zuo, H.; Liu, P.; Wen, Z. Experimental study on engine gas-path component fault monitoring using exhaust gas electrostatic signal. *Meas. Sci. Technol.* **2013**, *24*, 125107. [CrossRef]
18. Vatazhin, A.B.; Likhter, V.A.; Sepp, V.A.; Shul'gin, V.I. Effect of an electric field on the nitrogen oxide emission and structure of a laminar propane diffusion flame. *Fluid Dyn.* **1995**, *30*, 166–174. [CrossRef]
19. Vatazhin, A.B.; Golentsov, D.A.; Likhter, V.A.; Shulgin, V.I. Aircraft engine state nonobstructive electrostatic monitoring: Theoretical and laboratory modelling. *J. Electrost.* **1997**, *40–41*, 711–716. [CrossRef]

20. Sorokin, A.; Arnold, F. Electrically charged small soot particles in the exhaust of an aircraft gas-turbine engine combustor: Comparison of model and experiment. *Atmos. Environ.* **2004**, *38*, 2611–2618. [CrossRef]
21. Tang, X.; Chen, Z.-S.; Li, Y.; Hu, Z.; Yang, Y.-M. Analysis of the dynamic sensitivity of hemisphere-shaped electrostatic sensors' circular array for charged particle monitoring. *Sensors* **2016**, *16*, 1403. [CrossRef] [PubMed]
22. Tajdari, T.; Rahmat, M.F.A.; Wahab, N.A. New technique to measure particle size using electrostatic sensor. *J. Electrost.* **2014**, *72*, 120–128. [CrossRef]
23. Wang, L.; Yan, Y.; Hu, Y.; Qian, X. Rotational speed measurement using single and dual electrostatic sensors. *IEEE Sens. J.* **2014**, *15*, 1784–1793. [CrossRef]
24. Addabbo, T.; Fort, A.; Mugnaini, M.; Panzardi, E.; Vignoli, V. A Smart Measurement System with Improved Low-Frequency Response to Detect Moving Charged Debris. *IEEE Trans. Instrum. Meas.* **2016**, *65*, 1874–1883. [CrossRef]
25. Addabbo, T.; Fort, A.; Mugnaini, M.; Panzardi, E.; Vignoli, V. Measurement System Based on Electrostatic Sensors to Detect Moving Charged Debris with Planar-Isotropic Accuracy. *IEEE Trans. Instrum. Meas.* **2019**, *68*, 837–844. [CrossRef]
26. Wilcox, M.; Ransom, D.; Henry, M.; Platt, J. Engine distress detection in gas turbines with electrostatic sensors. In Proceedings of the Turbo Expo: Power for Land, Sea, and Air, Glasgow, UK, 14–18 June 2010; pp. 39–51.
27. Powrie, H.; Fisher, C. Engine health monitoring: Towards total prognostics. In Proceedings of the 1999 IEEE Aerospace Conference. Proceedings (Cat. No. 99TH8403), Snowmass, CO, USA, 7 March 1999; pp. 11–20.
28. Powrie, H.; Fisher, C. Monitoring of foreign objects ingested into the intake of a gas turbine aero-engine. In *International Conference on Condition Monitoring Proceedings*; University of Swansea: Swansea, UK, 1999; pp. 175–190.
29. Fisher, C. Data and information fusion for gas path debris monitoring. In Proceedings of the 2001 IEEE Aerospace Conference Proceedings (Cat. No. 01TH8542), Big Sky, MT, USA, 10–17 March 2001; pp. 3017–3022.
30. Powrie, H.; Novis, A. Gas path debris monitoring for F-35 joint strike fighter propulsion system PHM. In Proceedings of the 2006 IEEE Aerospace Conference, Big Sky, MT, USA, 4–11 March 2006; p. 8.
31. Dunn, R.; Wright, A.; Hudson, M. Charged particle detection in rocket plumes for monitoring engine distress. *Int. J. Turbo Jet Engines* **1999**, *16*, 255–262. [CrossRef]
32. Dunn, R.; Wright, A.; Bryant, C.; Mack, H.; Hudson, M.; Dunn, A. Noninvasive ion detection in rocket plumes for health monitoring. In Proceedings of the 36th AIAA/ASME/SAE/ASEE Joint Propulsion Conference and Exhibit, Las Vegas, NV, USA, 24–28 July 2000; p. 3884.
33. Wen, Z.; Hou, J.; Jiang, Z. Formation mechanism analysis and detection of charged particles in an aero-engine gas path. *Int. J. Aeronaut. Space Sci.* **2015**, *16*, 247–253.
34. Wen, Z.; Ma, X.; Zuo, H. Characteristics analysis and experiment verification of electrostatic sensor for aero-engine exhaust gas monitoring. *Measurement* **2014**, *47*, 633–644. [CrossRef]
35. Powrie, H.; Worsfold, J. Gas path debris monitoring for heavy-duty gas turbines-a pilot study. In *IDGTE Gas Turbine Symposium*; IDGTE: Bedford, UK, 2001; pp. 168–179.
36. Tian, Z.; Lu, P.; Grundy, J.; Harvey, T.; Powrie, H.; Wood, R.J.S.; Physical, A.A. Charge pattern detection through electrostatic array sensing. *Sens. Actuators A Phys.* **2024**, *371*, 115295. [CrossRef]
37. Sun, J.; Wood, R.J.K.; Wang, L.; Care, I.; Powrie, H.E.G. Wear monitoring of bearing steel using electrostatic and acoustic emission techniques. *Wear* **2005**, *259*, 1482–1489. [CrossRef]
38. Yan, Y.; Byrne, B.; Woodhead, S.; Coulthard, J. Velocity measurement of pneumatically conveyed solids using electrodynamic sensors. *Meas. Sci. Technol.* **1995**, *6*, 515–537. [CrossRef]
39. Powrie, H.; McNicholas, K.; Powrie, H.; McNicholas, K. Gas path monitoring during accelerated mission testing of a demonstrator engine. In Proceedings of the 33rd Joint Propulsion Conference and Exhibit, Seattle, WA, USA, 6–9 July 1997.
40. Sorokin, A.; Arnold, F. Organic positive ions in aircraft gas-turbine engine exhaust. *Atmos. Environ.* **2006**, *40*, 6077–6087. [CrossRef]
41. Haverkamp, H.; Wilhelm, S.; Sorokin, A.; Arnold, F. Positive and negative ion measurements in jet aircraft engine exhaust: Concentrations, sizes and implications for aerosol formation. *Atmos. Environ.* **2004**, *38*, 2879–2884. [CrossRef]
42. Sorokin, A.; Vancassel, X.; Mirabel, P. Emission of ions and charged soot particles by aircraft engines. *Atmos. Chem. Phys.* **2003**, *3*, 325–334. [CrossRef]
43. Yin, Y.; Zuo, H.; Wen, Z.; Cai, J.; Fu, Y. Electrostatic induction characteristics of aeroengine inhaled particles: Simulated experiment and analysis. *Hangkong Xuebao/Acta Aeronaut. Astronaut. Sin.* **2015**, *36*, 691–702. [CrossRef]
44. Sun, J.; Jiang, H.; Yang, C.; Liu, R. Characterization of gas turbine ingested sand particles based on electrostatic signal. *Proc. Inst. Mech. Eng. Part A J. Power Energy* **2022**, *236*, 463–476. [CrossRef]
45. Sun, J.; Jiang, H.; Chen, Y. Aero engine sand dust ingestion electrostatic monitoring simulation experiment. *J. Aerosp. Power* **2018**, *33*, 2913–2923. [CrossRef]
46. Sun, J.; Liu, X.; Liu, R.; Kang, Y.; Yin, Y.; Zuo, H. IDMS based method for quantitative monitoring of aero-engine ingested airborne sands. *Hangkong Xuebao/Acta Aeronaut. Astronaut. Sin.* **2017**, *38*. [CrossRef]
47. Wen, Z.; Zuo, H.; Pecht, M.G. Electrostatic Monitoring of Gas Path Debris for Aero-engines. *IEEE Trans. Reliab.* **2011**, *60*, 33–40. [CrossRef]
48. Hussain, T.; Kaialy, W.; Deng, T.; Bradley, M.S.; Nokhodchi, A.; Armour-Chelu, D. A novel sensing technique for measurement of magnitude and polarity of electrostatic charge distribution across individual particles. *Int. J. Pharm.* **2013**, *441*, 781–789. [CrossRef]

49. Pengpeng, L.; Hongfu, Z.; Jianzhong, S. The Electrostatic Sensor Applied to the Online Monitoring Experiments of Combustor Carbon Deposition Fault in Aero-Engine. *IEEE Sens. J.* **2014**, *14*, 686–694. [CrossRef]
50. Torres, M.E.; Colominas, M.A.; Schlotthauer, G.; Flandrin, P. A complete ensemble empirical mode decomposition with adaptive noise. In Proceedings of the 2011 IEEE International Conference on Acoustics, Speech and Signal Processing (ICASSP), Prague, Czech Republic, 22–27 May 2011; pp. 4144–4147.
51. Liu, Y.; Liu, Z.; Zuo, H.; Jiang, H.; Li, P.; Li, X. A DLSTM-Network-Based Approach for Mechanical Remaining Useful Life Prediction. *Sensors* **2022**, *22*, 5680. [CrossRef] [PubMed]
52. Zhong, Z.; Zuo, H.; Jiang, H. A nonlinear total variation based denoising method for electrostatic signal of low signal-to-noise ratio. *Adv. Mech. Eng.* **2022**, *14*, 16878132221136942. [CrossRef]

Disclaimer/Publisher's Note: The statements, opinions and data contained in all publications are solely those of the individual author(s) and contributor(s) and not of MDPI and/or the editor(s). MDPI and/or the editor(s) disclaim responsibility for any injury to people or property resulting from any ideas, methods, instructions or products referred to in the content.